ELSEVIER

Contents lists available at ScienceDirect

# Applied Catalysis B: Environment and Energy

journal homepage: www.elsevier.com/locate/apcatb





# Dual-functional heterojunction catalyst for synergistic improvement in selectivity of CO<sub>2</sub> electroreduction for continuous production of high-concentration liquid fuels over a broad voltage range

Zhaolin Shi <sup>a,1</sup>, Chao Zhang <sup>a,1</sup>, Hongjuan Wang <sup>a,1</sup>, Zhouru Ji <sup>a</sup>, Mengyu Qi <sup>a</sup>, Simeng Liu <sup>a</sup>, Weiqi Wang <sup>a</sup>, Chen Chen <sup>b</sup>, Jiqing Jiao <sup>a,\*</sup>, Tongbu Lu <sup>a,\*</sup>

#### ARTICLE INFO

# Keywords: Dual-functional heterojunction catalyst High concentration Continuous production Electrocatalytic $\mathrm{CO}_2$ reduction Liquid fuels

#### ABSTRACT

Continuous production of liquid fuels in high concentration via electrocatalytic  $CO_2$  reduction ( $CO_2RR$ ) calls for high-selectivity electrocatalysts and advanced devices. Here we designed and constructed a dual-functional heterojunction catalyst with an in situ growth strategy. The dual-functional heterojunction catalyst could synergistically activate  $CO_2$  and water (as confirmed via in situ spectroscopy and theoretical calculations), and therefore the catalyst displayed a high selectivity and activity for formate production. Equipped with this catalyst, our custom-built gas—membrane—liquid electrolytic cell could continuously produce formate with a concentration as high as 1.55-1.85 M over the voltage range from 2.8 to 3.4 V (reaching the maximum of 1.85 M at 3.1 V). For continuous production of high-concentration HCOOH via  $CO_2RR$ , our system features a broad voltage window. The results of theoretical calculations and in situ spectroscopies collectively demonstrate that constructing dual-functional heterojunction catalyst that work in synergy is the key solution to improving the overall catalytic performance.

#### 1. Introduction

Electrocatalytic  $CO_2$  reduction ( $CO_2RR$ ), when powered by renewable energies (such as solar and wind), could produce value-added commodity chemicals and help to neutralize the anthropogenic carbon emission. Owing to the intermittency of renewable energy, the production of liquid fuels with high concentration via  $CO_2RR$  calls for high-selectivity electrocatalysts working across broad potential windows. Because of the high chemical inertness of  $CO_2$  molecules, the activation of  $CO_2$  in  $CO_2RR$  is rather difficult, typically resulting in low conversions [1–4]. The most efficient pathways for  $CO_2RR$  have been recognized as the two-electron reduction to  $CO_2$  and  $CO_2RR$  have been recognized as higher volumetric energy density and could be more easily separated, stored and distributed [8–14]. Bismuth (Bi)-based catalysts have been known capable of producing HCOOH [15–19], but they generally suffer from relatively low activities and narrow potential windows for selective

HCOOH production [20–22]. In determining the selectivity during  ${\rm CO_2RR}$  process, the behavior of interfacial water plays a major role. It has been reported that introduction of a second active site may not only promote water activation to increase local proton concentration for  ${\rm CO_2}$  reduction, but also stabilize the key intermediates [23–27]. Therefore, constructing dual-functional catalysts that could synergistically activate both water and  ${\rm CO_2}$  molecules is expected to effectively optimize the catalytic selectivity and the activity [28–31].

Recently, Wang et al. employed a solid-state electrolyte (SSE) for  $CO_2RR$  and obtained pure HCOOH product, and they also reported that 0.1 M HCOOH solution could be generated consistently in continuous production [32]. In a following work, the team devised an all-solid-state electrocatalytic  $CO_2RR$  system and achieved continuous production of HCOOH [33]. Zeng et al. reported continuous production of a pure formic acid solution using a single-atom Pb-alloyed Cu catalyst via SSE [34]. Xia et al. also demonstrated continuous production of  $\sim$ 0.12 M HCOOH solution in a SSE-mediated reactor (at a current density of

E-mail addresses: jiaojiqing101@163.com (J. Jiao), lutongbu@tjut.edu.cn (T. Lu).

<sup>&</sup>lt;sup>a</sup> International Joint Laboratory of Materials Microstructure, Institute for New Energy Materials and Low Carbon Technologies, Analysis and Testing Center, School of Materials Science and Engineering, Tianjin University of Technology, Tianjin 300384, China

b Engineering Research Center of Advanced Rare Earth Materials, Department of Chemistry, Tsinghua University, Beijing 100084, China

<sup>\*</sup> Corresponding authors.

 $<sup>^{1}\,</sup>$  These authors contributed equally.

 $30~\text{mA}~\text{cm}^{-2})$  [9]. Wang et al. synthesized a Bi<sub>2</sub>S<sub>3</sub>-derived catalyst and achieved continuous production of 3.5 M HCOOH solution with a SSE-based reactor [35]. Despite the notable advantages of SSE, the related devices need to be further optimized in the following aspects. First, The SSE poses additional ohmic resistance that could lower the reactor's overall energy efficiency; second, the transport of generated products into SSE is driven by both the electric field and the concentration gradient across membranes, which may negatively influence the selectivity and the concentration of liquid products. Therefore, it is still a challenging task to design high-performance catalyst and novel catalytic reactors for direct production of high-concentration liquid fuels via  $CO_2RR$ .

Here, we constructed dual-functional heterojunction catalyst Bi/  $CeO_{2-x}$ , in which Bi helps to activate  $CO_2$ , and  $CeO_{2-x}$  is responsible for water activation. The dual-functional heterojunction catalyst could synergistically activate CO2 and water, and therefore displayed a high selectivity over a broad potential window (the Faradaic efficiency for formate reaching > 90 %). The dual-functional heterojunction catalyst was then incorporated into a custom-built gas-membrane-liquid (GML) electrolytic cell, which features a simplified assembly structure, and the fast mass transport characteristic of flow cells, as well as the easy gas-liquid separation characteristic of SSE-based reactors. Equipped with this high-selectivity catalyst, our GML cell could produce formate with a concentration as high as 1.55-1.85 M over the voltage range. The results of theoretical calculation and in situ spectroscopy collectively that constructing dual-functional heterojunction catalyst that work in synergy is the key solution to improving the overall catalytic performance.

#### 2. Experimental section

#### 2.1. Chemicals

Bismuth nitrate pentahydrate (Bi(NO<sub>3</sub>)<sub>3</sub>•5H<sub>2</sub>O, Innochem, 99 %), urea (CH<sub>4</sub>N<sub>2</sub>O, Aladdin, 99 %), cerium(III) nitrate hexahydrate (Ce (NO<sub>3</sub>)<sub>3</sub>•6H<sub>2</sub>O, Innochem, 99 %), hexadecyl trimethyl ammonium bromide (C<sub>19</sub>H<sub>42</sub>BrN, Innochem, 99 %), ethanol (C<sub>2</sub>H<sub>5</sub>OH, Fuchen, AR), acetone (C<sub>3</sub>H<sub>6</sub>O, Fuchen, AR), potassium bicarbonate (KHCO<sub>3</sub>, Aladdin, 99.5 %), potassium sulphate (K<sub>2</sub>SO<sub>4</sub>, Aladdin, 99 %), sulfuric acid (H<sub>2</sub>SO<sub>4</sub>, Fuchen, 95 %), nitric acid (HNO<sub>3</sub>, Beijing Chemical Works, 36–37 %), proton exchange membrane (Nafion 117, Sigma-Aldrich, 5 wt %), anionic exchange membrane (FAA-3-PK-130), deuterated water (D<sub>2</sub>O, Aladdin, 99 %), dimethyl sulfoxide (DMSO, Aladdin, 99.99 %), sodium hydroxide (NaOH, 85 %) were purchased from commercial sources. Ag/AgCl reference electrode and Pt wire electrode were obtained from Gaoss Union. Deionized water (DI-H<sub>2</sub>O) was obtained from a distilling apparatus. All the electrochemical experiments were conducted with a electrochemical workstation (Chenhua, Shanghai).

#### 2.2. Preparation of Bi/CeO<sub>2-x</sub>

The purchased commercial carbon cloth was cut into the pieces  $2\times 2$  cm in size. The carbon cloth was placed in 500 mL three-necked flask and ultrasonicated in acetone, ethanol and deionized water for 10 min sequentially. Then, the pieces of carbon cloth were heated in concentrated HNO<sub>3</sub> at  $100\,^{\circ}\text{C}$  for 1 h, washed with deionized water, and dried in vacuum at  $60\,^{\circ}\text{C}$  for 12 h. In a typical gram-scale synthesis, Bi (NO<sub>3</sub>)<sub>3</sub>•5H<sub>2</sub>O (970 mg), Ce(NO<sub>3</sub>)<sub>3</sub>•6H<sub>2</sub>O (52.1 mg) and C<sub>19</sub>H<sub>42</sub>BrN (500 mg) were dissolved in 60 mL water, and an ethanol solution (40 mL) of urea (3.0 g) was added. The mixture was stirred for 30 min, and then kept under 90 °C for 4 h; subsequently, a piece of carbon cloth (2 × 2 cm²) was immersed in the mixture, which was further stirred and cooled down to room temperature. The carbon cloth thus obtained was rinsed thrice with a mixed solvent ( $V_{\text{EtOH}}$ :  $V_{\text{water}} = 1:1$ ), dried in vacuum at  $60\,^{\circ}\text{C}$ , and then subjected to pyrolysis at 700 °C (ramping rate, 5 °C min<sup>-1</sup>) in N<sub>2</sub> atmosphere for 2 h. The black catalyst Bi/CeO<sub>2-x</sub> was

deposited on carbon cloth via in situ synthesis. The  $Bi/CeO_{2-x}$  (low) and  $Bi/CeO_{2-x}$  (high) catalysts were prepared by the same method with different amounts of  $Ce(NO_3)_3 \bullet 6H_2O$  (26.1 mg and 104.2 mg, respectively) added.

#### 2.3. Characterizations

Transmission electron microscopy (TEM) was conducted using TECNAI G2 Spirit TWIN microscope at 120 kV. High-Resolution Transmission Electron Microscopy (HRTEM) was conducted using TALOS F200 X microscope at 120 kV. The X-ray diffraction (XRD) tests were carried on Japanese Science company SmartLab 9 KW (Cu K $\alpha$ , 40 kV, 150 mA,  $\lambda=1.54178$  Å) in the range of  $2\theta$  from 20° to 80°. The room-temperature CO<sub>2</sub> adsorption isotherms were recorded on BELSORP-Max equipment. X-ray photoelectron spectroscopy (XPS) results were obtained on Thermo scientific spectrometer (ESCALAB250Xi, Al K $\alpha$ ). Elemental analysis was carried out by inductively coupled plasma optical emission spectroscopy (ICP-MS, iCAP RQ).

#### 2.4. Electrochemical measurement

Electrocatalytic  $CO_2$  reduction in H-type cell. All the electrochemical measurements were performed with a CHI 660E (Chenhua, Shanghai) using a gas-tight two-compartment H-cell separated by a proton exchange membrane. The as-synthesized sample was loaded onto carbon cloth that served as the working electrode. Ag/AgCl (saturated KCl) and Pt foil were used as counter electrode and reference electrode, respectively. The two compartments were each filled with 20 mL of 0.5 M KHCO<sub>3</sub> electrolyte. The electrolyte was bubbled with ultrapure  $CO_2$  gas for 30 min prior to measurements (pH = 7.3). The LSV curves were recorded in  $CO_2$ -saturated and Ar-saturated 0.5 M KHCO<sub>3</sub> solution with the scan rate of 5 mV s<sup>-1</sup> in the H-cell system. All the potentials were referenced to reversible hydrogen electrode (RHE) using the equation below:

$$E_{RHE} = E_{Ag/AgCl} + 0.197 + 0.0591 \times pH$$
 (1)

EIS measurements were measured in  ${\rm CO_2}$ -saturated 0.5 M KHCO $_3$  aqueous solution over the frequency range 0.1–10 $^6$  Hz.

Electrocatalytic  $CO_2$  reduction in flow cell. The flow cell consists of a gas chamber, a catholyte chamber, and an anolyte chamber. Each chamber has an inlet and outlet for the feed of  $CO_2$  gas or for the circulation of electrolyte. The exposed window for electrode is  $2\times 2$  cm². 1 M KOH aqueous solution was used as both anolyte and catholyte, and the two chambers were separated with an anion exchange membrane (AEM). An electronic flowmeter was employed to control the flow rate of  $CO_2$  gas.

Electrocatalytic CO<sub>2</sub> reduction in GML. In the GML configuration, stainless steels with a serpentine channel served as the anodic current collector and cathodic current collector, and a proton exchange membrane served as the membrane. The catalyst was placed between the cathodic current collector and proton exchange membrane to serve as the cathode, and a platinum–titanium felt loaded IrO<sub>2</sub> was placed between the anode and proton exchange membrane to serve as the anode. The catalyst exposed area was 1 cm², and the carbon cloth was cut into  $2\times 2$  cm² for support and gas diffusion layer. Specifically, the cathode side was fed with humidified CO<sub>2</sub> gas (10 sccm). The anode was supplied with recirculated mixed electrolyte at a flow rate of 20 mL/min. The CO<sub>2</sub> was humidified by pouring 150 mL DI water into a 250 mL glass bottle kept at 80 °C. In order to collect the HCOOH liquid product, we added a condensing unit at the gas outlet.

#### 2.5. Product analysis

The gas products of electrolysis were detected on the Shimadzu gas chromatography equipped with a dual thermal conductivity detector and flame ionization detector system. High-purity Ar (99.9999 %) was used as the carrier gas for the chromatography. The liquid products of electrocatalytic reduction of  $CO_2$  were determined via  $^1H$  nuclear magnetic resonance (NMR) spectroscopy (Avance III 400 MHZ, Bruker, Germany), and formate was found as the only liquid product. In detail, 450  $\mu$ L of electrolyte after reaction was collected and mixed with 50  $\mu$ L of  $D_2O$  and DMSO as the internal reference.

Calculation method: The faradaic efficiency of each reduction product was calculated according to the following equation:

$$FE_{gas} \quad (\%) = \frac{nNF}{Q_{total}} \times 100\% \tag{2}$$

*n*: the molarity of the product, mol;

 $\it N$ : the number of electron transferred for product formation, which is 2 for both HCOOH, CO and  $\it H_2$  production;

F: Faraday's constant, 96,500 C mol<sup>-1</sup>;

 $Q_{total}$ : the total amount of electricity passed through an electrode during electrolysis, C.

For liquid products, the following method was used for the calculation of faradaic efficiency ( $FE_{liquid}$ ):

$$\text{FE}_{liquid} = \frac{q_l}{q_{tot}} \times 100\% = \frac{F \times c_l \times V_{cell} \times n_l}{q_{tot}} \times 100\% \tag{3}$$

where  $c_l$  (mol L<sup>-1</sup>) was the concentration of formate that was calculated from <sup>1</sup>H NMR spectroscopy, F was the Faraday constant,  $V_{\rm cell}$  (L) was the electrolyte volume in the cell, and  $q_{\rm tot}$  (C) was the passed total charge.

#### 2.6. In-situ ATR-SEIRAS measurements

All SEIRAS measurements were performed using a custom-made three-electrode cell, including an Au film as working electrode, Ag/AgCl as reference electrode, and a platinum wire as counter electrode. The catalyst (5 mg) was dispersed in Nafion solution (1 mL 5 %) to prepare the catalyst ink, then the catalyst ink was drop-cast onto the Au film surface. The  $\rm CO_2$  reduction reaction was conducted in  $\rm CO_2$ -saturated 0.5 M KHCO $_3$  electrolyte, the real-time SEIRAS spectra were simultaneously recorded using chronoamperometry ( $\it I-t$ ) at different potentials with potential swept from -0.9 to -1.3 V (vs. RHE) with a step width of 100 mV. All spectra were collected with a 4 cm $^{-1}$  spectral resolution.

#### 2.7. Finite-element analysis

The model of the serpentine flow channel at the cathodic part for finite-element analysis was constructed in COMSOL Multiphysics 6.1 as a three-dimensional model. The channel was set to be 1.5 mm in both height and width, and the serpentine shape was circumscribed in a square with an edge length of 20 mm.

The modules of "laminar flow" and "transport of dilute species" were employed to simulate the distribution of  $CO_2$  concentration along the flow channel. One end of the serpentine flow channel was set as the inlet, with a volume flow rate of 10 sccm for pure  $CO_2$  (g); the other end of the channel as set as the "fully developed flow" outlet with an average absolute pressure (p) of 1 atm. The bottom boundary was set as a "flux" boundary, with an outward normal  $CO_2$  molar flux (J) proportional to the current density ( $j = I/A_{\rm active}$ ; I standing for the total current, set to be 150 mA;  $A_{\rm active}$  standing for the active surface area), specifically, J = j\*FE/2F (FE standing for the Faradaic efficiency, set as 0.9; F standing for the Faraday constant). The flowing gas was assumed to be an ideal gas, obeying p = cRT (c standing for molar concentration, R for ideal gas constant, and T for temperature). The gas temperature was set as 323.15 K.

The governing equations for the laminar flow and the transport of  ${\rm CO}_2$  (g) are shown below:

$$\nabla \bullet \mathbf{V} = 0 \tag{4}$$

$$\nabla \bullet (\rho \mathbf{V} \mathbf{V}) = -\nabla p + \mu \nabla^2 \mathbf{V} \tag{5}$$

$$\nabla \bullet (c\mathbf{V} - D\nabla c) = 0 \tag{6}$$

in which **V** stands for the flow velocity, for the gas density, c for CO<sub>2</sub> (g) concentration, p for absolute pressure, for the dynamic viscosity of CO<sub>2</sub> (g), and p for the diffusivity of CO<sub>2</sub> (g) in N<sub>2</sub> (g).

A mesh comprising tetrahedral elements was used to discretize the computational domain, and a linear shape function was used for the finite-element analysis.

#### 2.8. DFT calculations

All the density functional theory (DFT) calculations were performed with the Vienna *ab initio* simulation package (VASP) [36,37]. The generalized gradient approximation (GGA) of Perdew–Burke–Ernzerhof (PBE) [38] functional was adopted for the electron exchange–correlation. And the projected augmented wave (PAW) method [39] was used to describe the electron-ion interaction. During the calculations, the valence states were expanded in a plane-wave basis set with a cutoff energy of 400 eV and the Bi(6s6p), Ce(5 s,5p,6 s,4 f,5d), O(2s2p), C(2s2p) and H(1 s) electrons were treated as the valence states.

For Bi(012), the computational model was a periodic slab with a  $(2 \times 3)$  surface unit cell, which contains four layers and 48 atoms. During the calculations, the top two layers were relaxed and the bottom two layers were frozen. For CeO<sub>2</sub> (111), the computational model was a periodic slab with a  $(2 \times 2)$  surface unit cell, which contains three layers and 36 atoms (12 Ce atoms and 24O atoms). During the calculations, the top two layers were relaxed and the bottom one layers were frozen. For Bi(012)/CeO<sub>2</sub>, a Ce<sub>6</sub>O<sub>12</sub> cluster is loaded on the Bi(012) surface to mimic the heterojunction catalyst. A 15 Å vacuum layers was set to the three computational model to avoid the interaction between two adjacent layers. And the Brillouin zone was sampled by a Monkhorst-Pack mesh with a  $2 \times 2 \times 1$  grid in the reciprocal space. To balance the computational cost and accuracy, the convergence tolerance was set to  $10^{-5}$  eV for energy variation and 0.03 eV/ Å for force on each atom. In addition, the DFT+U approach was applied to describe electron localization on the 4 f states of the Ce atoms and the value of the effective Hubbard U was set to 4.5 eV.

The Gibbs free energy for the intermediates in the reaction pathway were calculated based on the following equation:

$$G = E_{DFT} + E_{ZPE} + \int C_V dT - TS$$
 (7)

Where  $E_{DFT}$  is the electronic energy which is obtained directly from the DFT optimizations,  $E_{ZPE}$  is the zero-point vibrational energy,  $\int C_V dT$  is the heat capacity, T is the temperature (298.15 K), and S is the entropy.

### 3. Results and discussion

# 3.1. Synthesis and characterization of dual-functional heterojunction catalyst

Fig. 1a illustrates the procedure of in situ growth of the dual-functional Ce-modified Bi catalyst on carbon cloth. Fig. 1b shows the scanning electron microscopy (SEM) image of the bare carbon cloth; Fig. 1c reveals that uniform nanosheets of precursor (thickness, 5.5 nm) were in situ grown on the carbon fibers. (Fig. S1) After pyrolysis, uniform nanoparticles (average diameter, 100 nm) composed of multiple smaller particles were formed (Fig. 1d). We also found that without Ce added, the product after pyrolysis would aggregate into large particles (~10 mm) (Fig. S2). Fig. S3 shows the powder X-ray diffraction (XRD) pattern for the precursor nanosheets basic bismuth nitrate [40,41], and in the XRD pattern for the nanoparticles obtained after pyrolysis, the

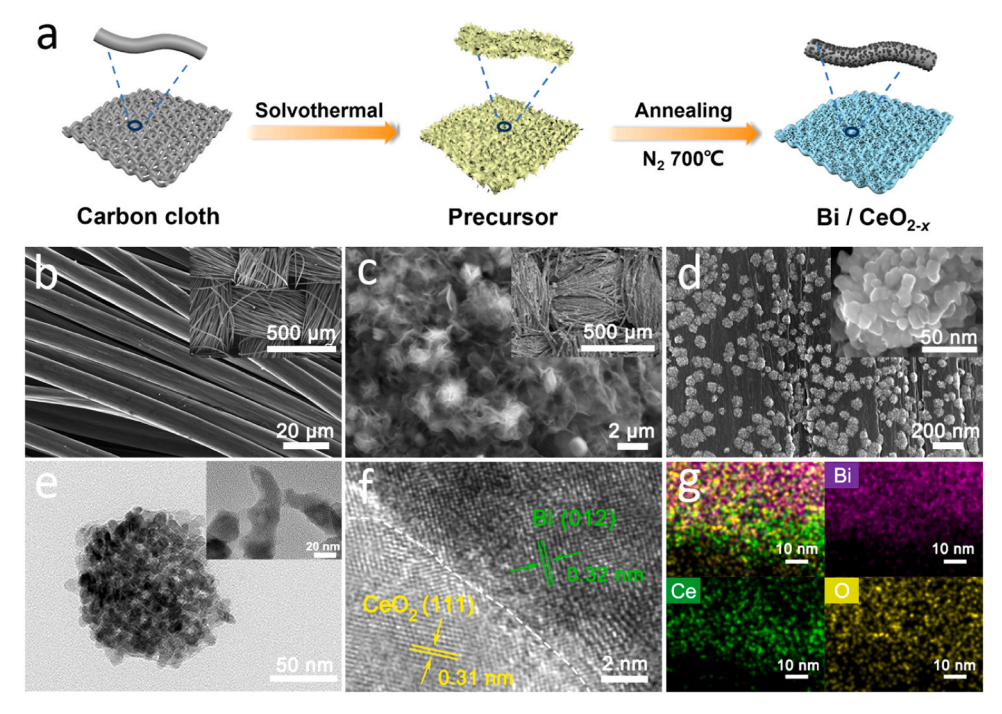


Fig. 1. Structural characterizations of dual-functional heterojunction catalyst. (a) Schematic illustration of the in situ growth of dual-functional heterojunction catalyst  $Bi/CeO_{2-x}$  on carbon cloth. (b–d) SEM images of carbon cloths: bare (b), with precursor (c) and with  $Bi/CeO_{2-x}$  (d). inset of (b) and (c): macroscopic form of carbon cloth, inset of (d): high-magnification SEM of  $Bi/CeO_{2-x}$ . TEM (e) and HRTEM (f) images for  $Bi/CeO_{2-x}$ . (g) EDS mapping for Bi, Ce and Ce elements.

major peaks are attributed to Bi (JCPDS No. 44-1246) [42], and the minor broader peaks are attributed to CeO<sub>2</sub> (JCPDS No. 34–0394) [27]. Fig. 1e shows the transmission electron microscopy (TEM) for the sample obtained after pyrolysis. Fig. 1f shows the high-resolution transmission electron microscopy (HRTEM) image corresponding to Fig. 1e. The interplanar distance is 0.32 nm, in accordance with Bi (012); the distance of crystal plane (gray range) is 0.31 nm, which is attributed to CeO2 (111). Energy-dispersive X-ray spectroscopy (EDS) elemental mapping reveals the uniform distribution of Bi and Ce elements, and the actual metal contents were for Ce (determined via ICP-MS) (Table S1). In order to investigate the chemical composition and electronic structure of the Bi/CeO<sub>2-x</sub> catalyst, X-ray photoelectron spectroscopy (XPS) was conducted [43,44]. Fig. 2a show the XPS survey spectra for the Ce-modified and unmodified samples; the elements of Bi, Ce, O and C were detected. Fig. 2b shows the Ce XPS profiles, and the ratios of  $Ce^{4+}$  and  $Ce^{3+}$  were determined to be ~58.7 % and ~41.3 %, respectively, indicating the formation of oxygen vacancies on the surface. Compared with the unmodified sample, the Bi/CeO<sub>2-x</sub> catalyst has a higher ratio of oxygen vacancies (Fig. 2c). Furthermore, as shown in Fig. S4, the electron paramagnetic resonance (EPR) [9] data displayed a higher signal intensity than that for pure Bi (Fig. S5). As shown in Fig. 2d, the peaks at 164.6 and 159.3 eV are due to Bi<sup>3+</sup> species for Bi and Bi/CeO<sub>2-x</sub> samples, and two new peaks at 162.2 and 156.8 eV ascribed to metallic Bi are found in Bi/CeO<sub>2-x</sub>, indicating the electron structure of Bi was regulated after Ce modification.

To further confirm the elemental valence and electronic structures of Bi [45,46], synchrotron-radiation-based X-ray absorption fine structure (XAFS) at the Bi [15,47,48] L-edge was conducted for different samples. Fig. 2e shows the X-ray absorption near-edge structure (XANES) profiles for Bi/CeO<sub>2-x</sub> and Bi without Ce modification, the corresponding references including the Bi foil and Bi<sub>2</sub>O<sub>3</sub>. The absorption edge for Bi/CeO<sub>2-x</sub> is closed to that for Bi foil, indicating the formation of Bi. Its absorption edge is located at lower energy compared with that of Bi without Ce modification, implying a lower Bi oxidation state of the Bi/CeO<sub>2-x</sub>. The bond lengths were probed via extended X-ray absorption fine structure (EXAFS) (Fig. 2f). For Bi foil, Bi/CeO<sub>2-x</sub> and Bi without Ce modification, the radial distance space spectra  $\chi$ (R) show major and

broad peaks around  $\sim 3.00$  Å, which are attributed to the Bi–Bi scattering path. The minor peaks at  $\sim 1.60$  Å are attributed to the Bi–O scattering path. The intensity of this minor peak for Bi/CeO<sub>2-x</sub> is lower than that for Bi without Ce modification, indicating that the electrons would transfer to Bi from oxide support. The electron structure of Bi/CeO<sub>2-x</sub> could be regulated by introducing Ce. We also found that the Bi/CeO<sub>2-x</sub> catalyst has a higher adsorption capacity for CO<sub>2</sub> than the unmodified counterpart, as revealed in CO<sub>2</sub> adsorption isotherms (Fig. S6).

### 3.2. Assessment of CO<sub>2</sub>RR performance

The CO<sub>2</sub>RR performances of the catalysts were assessed first using a standard three-electrode setup in an H-type cell [40], with CO<sub>2</sub>-saturated 0.5 M KHCO3 solution as the electrolyte. The Ce content was varied so as to screen for the optimal composition. As shown in the linear sweep voltammetry (LSV) curves (Fig. 3a), the introduction of Ce could significantly improve the catalytic activity. When the nominal Ce content was 6 % (denoted as Bi/CeO<sub>2-x</sub>), the catalyst gives the lowest onset potential and the highest current density for CO2RR. The LSV curves recorded in Ar- and CO2- saturated KHCO3 solutions are shown in Fig. S7. All the products were monitored via on-line gas chromatography (GC) or <sup>1</sup>H nuclear magnetic resonance (NMR) spectroscopy (Fig. S8,  $^{\rm S9}$ ). The  $^{\rm 13}$ C isotope experiments verifies that HCOOH is produced from CO<sub>2</sub> gas (Fig. S10) [49,50]. Compared with pristine Bi, the Ce-modified samples give an improved FE<sub>HCOOH</sub>. The performances of Ce-modified Bi samples with different nominal Ce contents (3 % and 12 %; denoted as Bi/CeO<sub>2-x</sub> (low) and Bi/CeO<sub>2-x</sub> (high), respectively) can be found in Fig. 3b. When the nominal Ce content was 6 % (Bi/CeO<sub>2-x</sub>), the  $FE_{HCOOH}$ is above 90 % over the potential range from  $-0.8 \sim -1.2$  V, and reaches the maximum of 97 % at -0.95 V. (Fig. 3b and Fig. S11,S12) The partial current densities for HCOOH ( $j_{\mbox{\scriptsize HCOOH}}$ ) are summarized in Fig. 3c. The jHCOOH of Bi/CeO2-x is higher than other samples over the entire potential ranges.Furthermore, the Tafel slope for Bi/CeO<sub>2-x</sub> was determined to be 113.8 mV dec<sup>-1</sup> (Fig. 3d), in contrast to 273.4 mV dec<sup>-1</sup> for Bi,  $190.2 \text{ mV dec}^{-1}$  for Bi/CeO<sub>2-x</sub> (low), and  $234.6 \text{ mV dec}^{-1}$  for Bi/CeO<sub>2-x</sub> (high). These data revealed that Bi/CeO<sub>2-x</sub> displays a

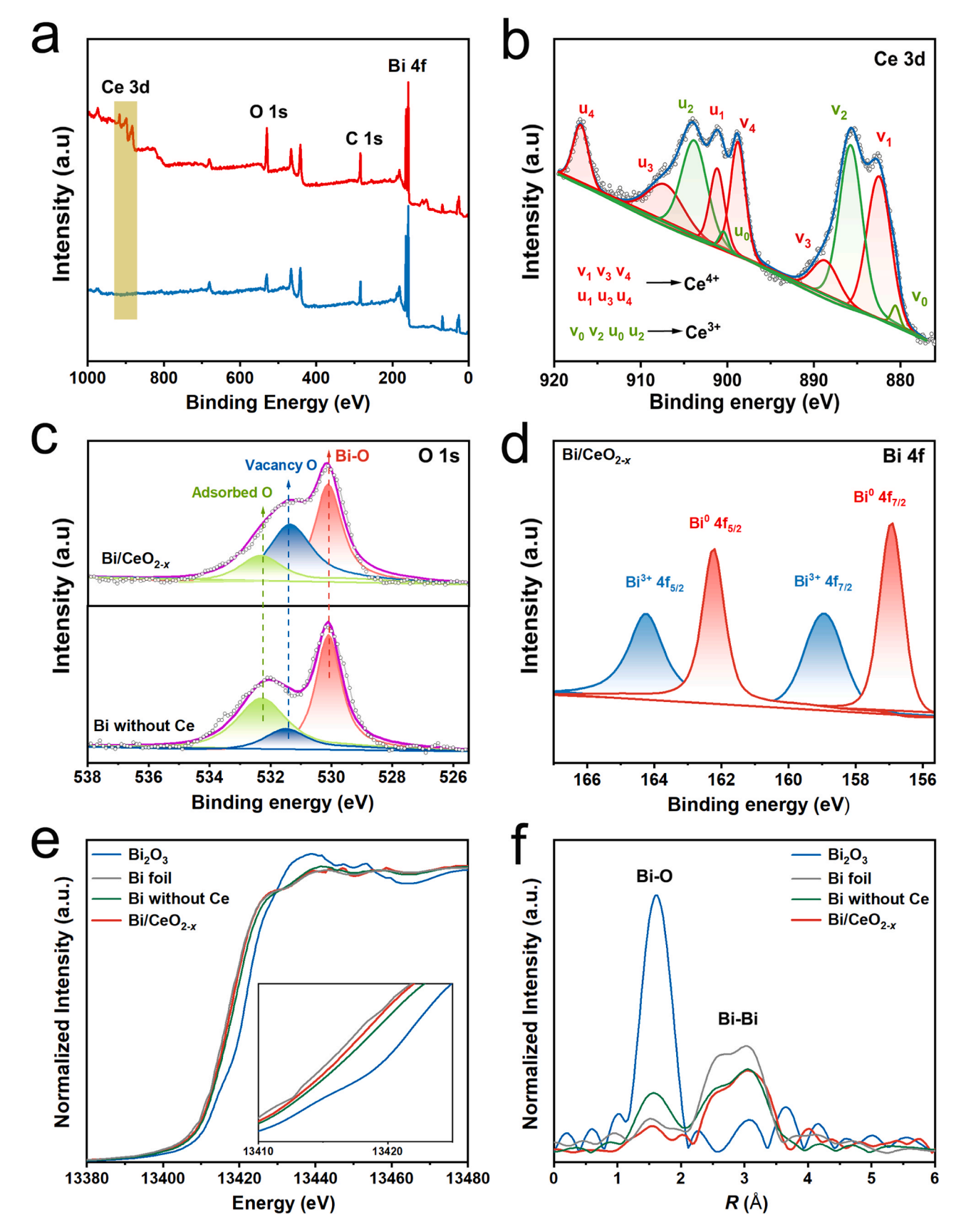


Fig. 2. XPS and XAFS spectroscopy analysis for catalysts. (a) XPS survey spectra; (b–d) high-resolution XPS profiles of (b) Ce 3d, (c) O 1s and Bi 4f for Bi/CeO<sub>2-x</sub> and Bi (d). (e, f) Normalized XANES  $\chi$ (E) spectra (Inset: Magnified absorption edge) and Radial distance  $\chi$ (R) space spectra of Bi for Bi/CeO<sub>2-x</sub> and Bi without Ce modification.

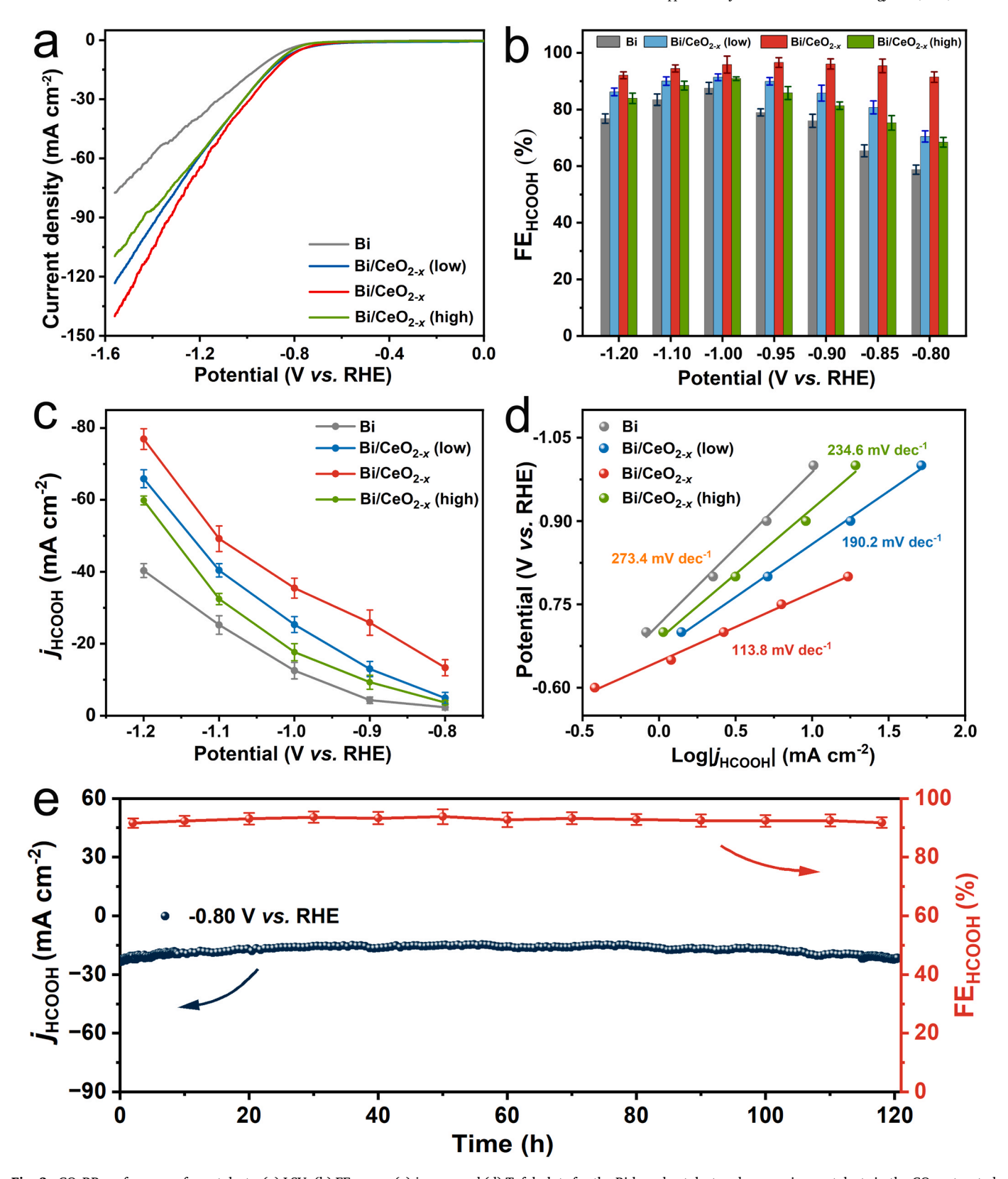


Fig. 3.  $CO_2RR$  performance for catalysts. (a) LSV, (b)  $FE_{HCOOH}$ , (c)  $j_{HCOOH}$  and (d) Tafel plots for the Bi-based catalyst and comparison catalysts in the  $CO_2$ -saturated in H-type cell. (e) i-t stability of the Bi/ $CeO_{2-x}$  at -0.8 V (vs. RHE) and the corresponding  $FE_{HCOOH}$ .

favorable reaction kinetics for producing HCOOH. The long-term stability and corresponding  $FE_{HCOOH}$  were assessed for 120 h for Bi/CeO<sub>2-x</sub> at -0.8 V (vs. RHE), and the results (Fig. 3e) indicate an excellent stability for CO<sub>2</sub>RR with high FE<sub>HCOOH</sub>. Over a broad voltage window,

Bi/CeO<sub>2-x</sub> displays a high catalytic performance.

Compared with previous reports, the obtained  $Bi/CeO_{2-x}$  displays a higher selectivity across a broad potential range for  $CO_2RR$ . Furthermore, the sample was also tested in flow cell configurations, and gave a

higher current density and stability (Fig. S13-S15).

#### 3.3. Continuous production of high-concentration formic acid

For the commonly used configurations of electrolytic cells (H-type cells and flow cells), the formate as product is inevitably dissolved in the electrolyte (typically in low concentrations), which also leads to substantial obstacles for the subsequent purification step. The SSE-based electrolyzers could yield products in high concentrations, but AEM, cation exchange membrane (CEM) and SSE are essential here, resulting in high ohmic resistance and significant joule heating during operation. In this work, we devised a new GML electrolyzer configuration specifically for CO<sub>2</sub>RR. Fig. S16 illustrates the configuration for the GML cell, which has only one ion exchange membrane inserted between the cathode and anode. The catalysts and the membrane are in direct contact, which could facilitate the mass transport and lower the ohmic resistance. The liquid product at the cathode could be readily carried out with the CO<sub>2</sub> gas flow, and subsequently collected with high concentration (Fig. S17,18). The high-selectivity catalyst Bi/CeO<sub>2-x</sub> was used for the test on the GML cell that we designed here. Humidified CO2 feed gas would be reduced at the cathode. Oxygen evolution reaction proceeds at the anode comprising Ti support loaded with IrO2. A mixture solution of  $0.5\ M\ K_2SO_4$  and  $0.01\ M\ H_2SO_4$  was used as the anolyte. At the surface of the Bi/CeO<sub>2-x</sub> catalyst, CO<sub>2</sub> was converted into HCOOH, which was then carried out by the gas flow, and subsequently condensed into formic acid solution in high concentration. The LSV curve(Fig. S19) demonstrates that the cell delivers high current densities under relatively low voltages, probably because of the lower ohmic resistance and faster mass transport compared with that of SSE-based counterparts. We further conducted finite-element analysis on the flow channel at the cathodic part during CO2RR. The simulated distribution of CO2 concentration is displayed in Fig. 4b and Fig. S20, a steady decrease in CO2 concentration could be noted along the flow path. The performance of carbon cloth, pristine CeO2, and Bi without Ce are summarized in Fig. S21. Fig. 4c summarizes the selectivity for HCOOH determined at different applied voltages. The  $j_{HCOOH}$  values were calculated at different voltages. Over the voltage range from 2.8 V to 3.4 V, the

selectivity for HCOOH is as high as > 90 %. The produced HCOOH solution was collected at different voltages, and the concentration in continuous production was found to be as high as 1.55–1.85 M, and reached the maximum of 1.85 M at 3.1 V. (Fig. 4d). The concentrations of HCOOH solutions collected at the outlet were found lower using different electrolytes (Fig. S22). The current density reaches 215 mA cm $^{-2}$  at 3.1 V. Stability test over 120 h revealed no significant decline in both selectivity and current density. (Fig. 4e). The HAADF-STEM and XPS characterizations in Fig. 23 and 24 demonstrate that the structural features of the catalyst remain well preserved after long-term electrolysis. To the best of our knowledge, as shown in Fig. 4f and Table S2, the HCOOH concentration obtained here is among the highest rank for continuous production, and the voltage range is also the broadest.

#### 3.4. Theoretical simulations and in situ spectroscopic characterizations

To gain further insights into the high efficiency in CO<sub>2</sub>RR to formate on Bi(012)/CeO2, we performed density functional theory (DFT) calculations. Considering the above experimental results, the calculation models for Bi(012), CeO<sub>2</sub> and Bi(012)/CeO<sub>2</sub> were constructed, and the corresponding adsorption configurations for the intermediates were investigated (Fig. 5a and Fig. S25). For Bi(012)/CeO2, the O atoms at the interface can form strong Bi-O bonds with the surrounding Bi atoms, which would influence the electronic structure and result in different catalytic performances at the interface compared with the individual surfaces. The current consensus regarding the mechanism of CO2 reduction to HCOOH is that the CO2 molecule has to be converted to the adsorbed \*OCHO intermediate. Differential charge density with yellow and cyan colors represents positive and negative electron density isosurfaces. As shown in Fig. S26, it can be seen that  $\sim$ 0.53 electrons are transferred from Bi to CeO2, demonstrating significant charge transfer at the interfaces. Significant charge transfer occurs between the interfaces, which could affect the electronic structure of metal Bi and make it to be beneficial for HCOOH production. In this work, the reaction pathways for the CO<sub>2</sub>-to-HCOOH conversion on Bi(012), CeO<sub>2</sub> and Bi(012)/CeO<sub>2</sub> were considered, and the corresponding energy diagrams were

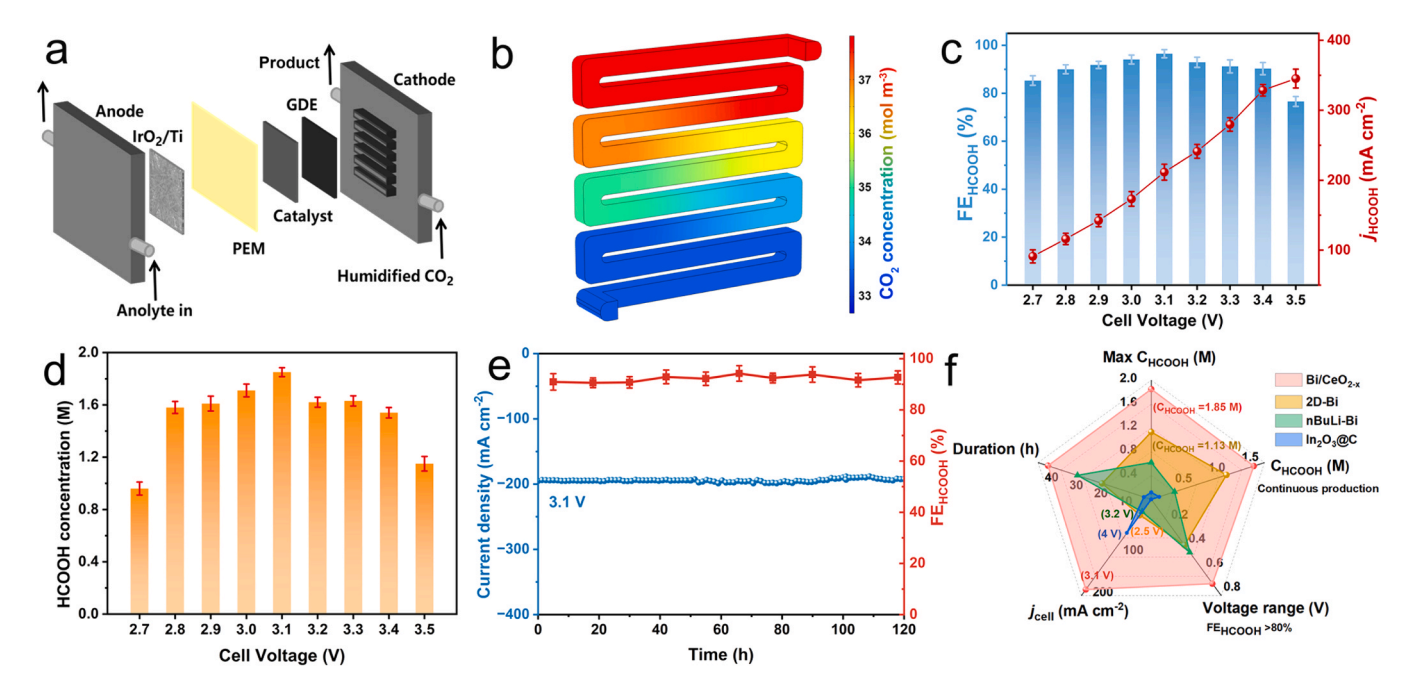


Fig. 4. Continuous production of formic acid using dual-functional heterojunction  $Bi/CeO_{2-x}$  catalyst. (a) Schematic illustration of the GML configuration. (b) Simulated distribution of  $CO_2$  concentration along the flow channel (assuming FE = 90 %). (c)  $FE_{HCOOH}$ , (d) Concentration of liquid product. (e) i-t stability of the  $Bi/CeO_{2-x}$  at 3.1 V and the corresponding  $FE_{HCOOH}$ . (f) Comparison of maximum (Max) HCOOH concentrations, continuous generation concentration, duration, partial current density and voltage range. (Inset: 2D-Bi [31], n-butyllithium-Bi [32] and  $In_2O_3@C$  [9]).

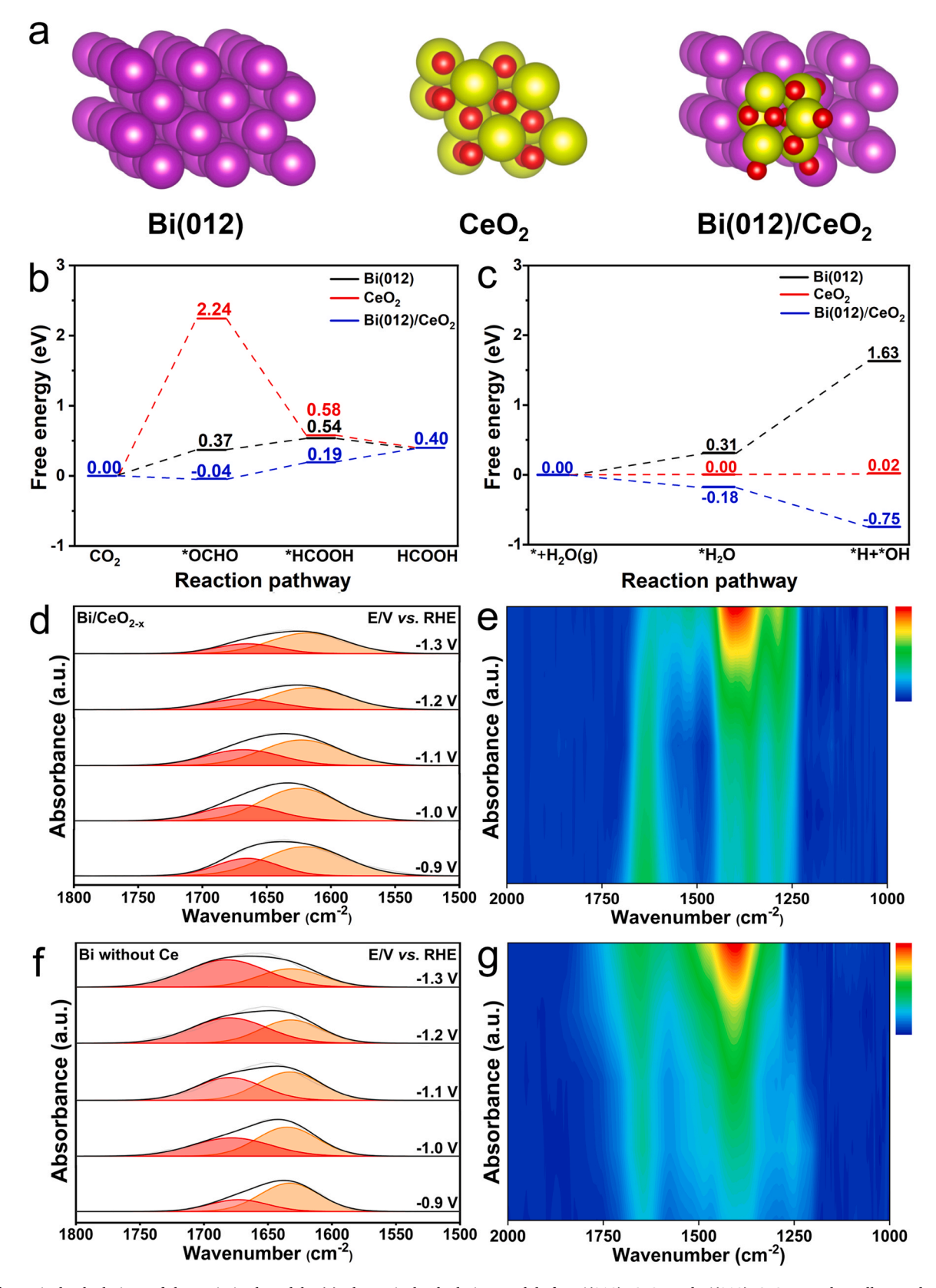


Fig. 5. Theoretical calculations of the optimized models. (a) Theoretical calculation models for Bi(012),  $CeO_2$  and Bi(012)/ $CeO_2$ . Purple, yellow and red spheres represent Bi, Ce and O atoms, respectively. (b, c) Gibbs free energy diagrams for  $CO_2$  reduction to HCOOH and  $H_2O$  dissociation on the Bi(012),  $CeO_2$  and Bi(012)/ $CeO_2$  models. (d, f) ATR-SEIRAS spectra collected on the surfaces of Bi/ $CeO_{2-x}$  and Bi. The fitted spectral profiles (black curves) reflecting the water bending mode and C=O stretching mode (pink, C=O stretching mode; orange, water bending mode). Corresponding contour maps of Bi/ $CeO_{2-x}$  (e) and Bi (g).

compared, and the asterisk represents the adsorption state (Fig. 5b, c). It can be seen that the Ce atom in CeO<sub>2</sub> cannot effectively adsorb the \*OCHO, because the formation of \*OCHO has a high free energy change value ( $\Delta G = 2.24$  eV), whereas the Bi atom in the pure Bi(012) surface and Bi(012)/CeO<sub>2</sub> could strongly stabilize the \*OCHO intermediate with a smaller  $\Delta G$  value of 0.37 eV and -0.04 eV, respectively. It should be noted that the introduction of CeO<sub>2</sub> onto the Bi(012) surface can further assist the CO<sub>2</sub> activation, and the formation of \*HCOOH is the rate-determining step with a  $\Delta G$  value of 0.23 eV. To probe the effect of Bi (012)/CeO<sub>2</sub> interface on H<sub>2</sub>O dissociation, the free energy diagram of H<sub>2</sub>O dissociation to \*H and \*OH species on Bi(012), CeO<sub>2</sub> and Bi(012)/CeO<sub>2</sub> were compared. It could be noted that the three models have similar adsorption properties for the H<sub>2</sub>O molecule with a  $\Delta G$  value of 0.31 eV, 0.00 eV and -0.18 eV, respectively.

In contrast, the H<sub>2</sub>O dissociation processes on the three models are significantly different. The formation of \*H and \*OH on Bi(012) and  $CeO_2$  is endothermic ( $\Delta G = 1.32$  eV and 0.02 eV), whereas this process on Bi(012)/CeO<sub>2</sub> interface is exothermic, and the  $\Delta G$  value remarkably decreases to - 0.57 eV. These results indicate that the CeO2 has a good performance in water activation, and the introduction of CeO<sub>2</sub> onto the Bi(012) surface can further accelerate H<sub>2</sub>O dissociation into \*H (which would participate in the CO<sub>2</sub> reduction) (Fig. S27). As shown in Fig. S28, the free energy changes for the rate-determining step for CO and H2 formation are 0.91 eV and 0.47 eV, respectively, both larger than that for HCOOH formation (0.23 eV), indicating that the competing CO and H<sub>2</sub> formation can be effectively suppressed during the CO<sub>2</sub>RR over Bi/ CeO2. As shown in Fig. S29, the free energy change for the ratedetermining step over Bi/CeO2 with oxygen vacancy is almost the same as that over Bi/CeO<sub>2</sub>, indicating the oxygen vacancy does not have decisive role in the CO2RR mechanism. On the basis of the above computational results, it can be concluded that the formation of the Bi (012)/CeO2 interface can not only promote the H2O dissociation, but also boost the CO2 reduction, which is well consistent with the experimental observations.

To experimentally verify the role of the dual-functional catalyst, insitu attenuated total reflection surface-enhanced infrared absorption spectroscopy (ATR-SEIRAS) was carried out to monitor the adsorbed species at the electrochemical interface(Fig. 5d-g). A band at 1665–1672 cm<sup>-1</sup> in the potential range from -0.9 to -1.3 V (vs. RHE) was found for both  $Bi/CeO_{2-x}$  and Bi catalysts, which is attributed to the C=O stretching mode in \*OCHO (a key intermediate to HCOOH). The peak intensity of the C=O stretching mode for the Bi/CeO<sub>2-x</sub> catalyst decreases with more negative potentials applied, indicating that the consumption rate of the intermediates increases, thus leading to a more rapid conversion to HCOOH. In contrast, the peak intensity of C=O stretching mode for the Bi catalyst increases with more negative potentials applied, indicating that the intermediates are accumulated at the interface, probably owing to the relatively slow reaction kinetics to HCOOH. In addition, another peak was found located in the 1620-1635 cm<sup>-1</sup> range, corresponding to the water bending mode. As shown in Fig. S30, the peak at ~1295 cm<sup>-1</sup> could be attributed to the C=O vibration of \*CO<sub>2</sub>, and the two peaks at 1408 cm<sup>-1</sup> and 1365 cm<sup>-1</sup> could be ascribed to the C-H bending and O-C-O symmetric vibrations of \*OCOH, a key intermediate for HCOOH formation [51,52]. Compared with Bi, the catalyst with CeO2 introduced displayed the favorable property for water dissociation. Thus, the dual-functional heterojunction catalyst  $\mathrm{Bi/CeO}_{2-x}$  could synergistically promote the formation of intermediates, thereby enhancing the overall catalytic performance.

#### 4. Conclusion

For continuous production of high-concentration HCOOH via  $CO_2RR$ , we designed and constructed dual-functional heterojunction catalyst  $Bi/CeO_{2-x}$  with an in situ growth strategy. The  $Bi/CeO_{2-x}$  displayed a high selectivity and activity for formate production in H-type cell and flow cell. The FE for formate reached > 90% ( $-0.8 \sim -1.2$  V vs.

RHE) in H-type cell. Equipped with dual-functional heterojunction catalyst, the custom-built GML cell could produce HCOOH with a concentration as high as 1.55–1.85 M over the voltage range from 2.8 to 3.4 V (the broadest reported thus far), and reached the maximum of 1.85 M at 3.1 V. ATR-SEIRAS revealed that the key intermediate could be readily generated on the dual-functional heterojunction catalyst Bi/CeO<sub>2-x</sub>. The results of theoretical calculations and in situ spectroscopies collectively demonstrate that constructing dual-functional heterojunction catalyst that work in synergy is the key solution to improving the overall catalytic performance. For continuous production of high-concentration HCOOH via CO<sub>2</sub>RR, our system features the broadest voltage window reported thus far, and our work here offers a promising solution to the practical application of CO<sub>2</sub>RR.

#### CRediT authorship contribution statement

Simeng Liu: Investigation. Weiqi Wang: Investigation. Chen Chen: Methodology. Jiqing Jiao: Writing – original draft, Project administration. Chao Zhang: Writing – review & editing, Methodology. Hongjuan Wang: Methodology. Zhouru Ji: Methodology. Mengyu Qi: Investigation. Zhaolin Shi: Methodology, Investigation. Tongbu Lu: Investigation.

#### **Declaration of Competing Interest**

The authors declare that they have no known competing financial interests or personal relationships that could have appeared to influence the work reported in this paper.

#### Acknowledgements

The work was financially supported by the National Key R&D Program of China (No. 2022YFA1502902), National Natural Science Foundation of China (No.52472236, No. 52072260, No.21931007, No.21790052 and No. U21A20317), Science and Technology Support Program for Youth Innovation in Universities of Shandong Province (No.2020KJA012), Tianjin Natural Science Foundation (21JCZXJC00130, B2021201074), Natural Science Foundation of Tianjin City (23JCQNJC00570), Haihe Laboratory of Sustainable Chemical Transformations. We acknowledge BL14W1 and BL11B beamline of Shanghai Synchrotron Radiation Facility (SSRF) Shanghai and 1W1B beamline of Beijing Synchrotron Radiation Facility (BSRF) Beijing (China) for providing the beam time.

# Appendix A. Supporting information

Supplementary data associated with this article can be found in the online version at doi:10.1016/j.apcatb.2025.125745.

## Data availability

No data was used for the research described in the article.

#### References

- [1] Y. Chen, X. Li, Z. Chen, A. Ozden, J.E. Huang, P. Ou, J. Dong, J. Zhang, C. Tian, B. Lee, X. Wang, S. Liu, Q. Qu, S. Wang, Y. Xu, R.K. Miao, Y. Zhao, Y. Liu, C. Qiu, J. Abed, H. Liu, H. Shin, D. Wang, Y. Li, D. Sinton, E.H. Sargent, Efficient multicarbon formation in acidic CO<sub>2</sub> reduction via tandem electrocatalysis, Nat. Nanotechnol. 19 (2024) 311–318, https://doi.org/10.1038/s41565-023-01543-8.
- [2] J. Chen, X. Zhu, Y. Yu, T. Huang, K. Zhang, Q. Luo, S. Gao, J. Yang, Stabilizing In/InN intermediates by electron-deficient carbon for improved CO<sub>2</sub> electroreduction to CO, Appl. Catal. B Environ. 361 (2025) 124668, https://doi.org/10.1016/j.apcatb.2024.124668.
- [3] Q. Zhang, J. Peng, S. Jiang, H. Xiong, X. Fu, S. Shang, J. Xu, G. He, P. Chen, Plasma-activated 2D CuMnO<sub>2</sub> nanosheet catalysts with rich oxygen vacancies for efficient CO<sub>2</sub> electroreduction, Appl. Catal. B Environ. 371 (2025) 125255, https://doi.org/10.1016/j.apcatb.2025.125255.

- [4] K. Sun, K. Yu, J. Fang, Z. Zhuang, X. Tan, Y. Wu, L. Zeng, Z. Zhuang, Y. Pan, C. Chen, Nature-inspired design of molybdenum-selenium dual-single-atom electrocatalysts for CO<sub>2</sub> reduction, Adv. Mater. 34 (2022) 2206478, https://doi. org/10.1002/adma.202206478.
- [5] D.M. Weekes, D.A. Salvatore, A. Reyes, A. Huang, C.P. Berlinguette, Electrolytic CO<sub>2</sub> reduction in a flow cell, Acc. Chem. Res. 51 (2018) 910–918, https://doi.org/ 10.1021/acs.accounts.8b00010.
- [6] M. Tan, X. Han, S. Ru, C. Zhang, Z. Ji, Z. Shi, G. Qiao, Y. Wang, R. Cui, Q. Luo, J. Jiao, Y. Li, T. Lu, Low-loading gold in situ doped with sulfur by biomolecule-assisted approach for promoted electrochemical carbon dioxide reduction, Nano Res. 16 (2023) 2059–2064, https://doi.org/10.1007/s12274-022-4878-3.
- [7] P. Sui, M. Zhu, M. Gao, Y. Wang, R. Feng, X. Wang, S. Liu, J. Luo, Energy-conservative CO<sub>2</sub> electroreduction for efficient formate co-generation, Appl. Catal. B Environ. 373 (2025) 125355, https://doi.org/10.1016/j.apcatb.2025.125355.
- [8] S. Yang, H. An, S. Arnouts, H. Wang, X. Yu, J. de Ruiter, S. Bals, T. Altantzis, B. M. Weckhuysen, W. van der Stam, Halide-guided active site exposure in bismuth electrocatalysts for selective CO<sub>2</sub> conversion into formic acid, Nat. Catal. 6 (2023) 796–806, https://doi.org/10.1038/s41929-023-01008-0.
- [9] Z. Wang, Y. Zhou, D. Liu, R. Qi, C. Xia, M. Li, B. You, B.Y. Xia, Carbon-confined indium oxides for efficient carbon dioxide reduction in a solid-state electrolyte flow cell, Angew. Chem. Int. Ed. 61 (2022) e202200552, https://doi.org/10.1002/ anie.202200552.
- [10] K. Chen, D. Ma, Y. Zhang, F. Wang, X. Yang, X. Wang, H. Zhang, X. Liu, R. Bao, K. Chu, Urea electrosynthesis from nitrate and CO<sub>2</sub> on diatomic alloys, Adv. Mater. 36 (2024) 2402160, https://doi.org/10.1002/adma.202402160.
- [11] S. Wang, L. Wang, X. Zhou, J. Fang, C. Deng, D. Wang, Design principles of singleatom catalysts anchored over porous materials for green catalysis and conversion, Nano Res. 18 (2025) 94907137, https://doi.org/10.26599/NR.2025.94907137.
- [12] R. Wang, J. Liu, Q. Huang, L. Dong, S. Li, Y. Lan, Partial coordination-perturbed Bicopper sites for selective electroreduction of CO<sub>2</sub> to hydrocarbons, Angew. Chem. Int. Ed. 60 (2021) 19829–19835, https://doi.org/10.1002/anie.202105343.
- [13] F. Yang, A.O. Elnabawy, R. Schimmenti, P. Song, J. Wang, Z. Peng, S. Yao, R. Deng, S. Song, Y. Lin, M. Mavrikakis, W. Xu, Bismuthene for highly efficient carbon dioxide electroreduction reaction, Nat. Commun. 11 (2020) 1088, https://doi.org/10.1038/s41467-020-14914-9.
- [14] E. Zhang, T. Wang, K. Yu, J. Liu, W. Chen, A. Li, H. Rong, R. Lin, S. Ji, X. Zheng, Y. Wang, L. Zheng, C. Chen, D. Wang, J. Zhang, Y. Li, Bismuth single atoms resulting from transformation of metal-organic frameworks and their use as electrocatalysts for CO<sub>2</sub> reduction, J. Am. Chem. Soc. 141 (2019) 16569–16573, https://doi.org/10.1021/jacs.9b08259.
- [15] Y. Kong, W. Wei, L. Xu, C. Chen, Electrochemical synthesis of organonitrogen compounds from N-integrated CO<sub>2</sub> reduction reaction, Acta Phys. Chim. Sin. 40 (2024) 2307049, https://doi.org/10.3866/pku.whxb202307049.
- [16] M. Qi, Y. Ma, C. Zhang, B. Li, X. Yang, Z. Shi, S. Liu, C. An, J. Jiao, T. Lu, High-selectivity electroreduction of low-concentration CO<sub>2</sub> with large concentration fluctuation, Sci. China Chem. 68 (2025) 1620–1626, https://doi.org/10.1007/s11426-024-2307-y.
- [17] C. Lin, Y. Liu, X. Kong, Z. Geng, J. Zeng, Electrodeposited highly-oriented bismuth microparticles for efficient CO<sub>2</sub> electroreduction into formate, Nano Res. 15 (2022) 10078–10083, https://doi.org/10.1007/s12274-022-4345-z.
- [18] P. Deng, H. Wang, R. Qi, J. Zhu, S. Chen, F. Yang, L. Zhou, K. Qi, H. Liu, B.Y. Xia, Bismuth oxides with enhanced bismuth-oxygen structure for efficient electrochemical reduction of carbon dioxide to formate, ACS Catal. 10 (2020) 743–750, https://doi.org/10.1021/acscatal.9b04043.
- [19] C.G. Bell, F. Gao, W. Yuan, L. Roos, R.J. Acton, Y. Xia, J. Bell, K. Ward, M. Mangino, P.G. Hysi, J. Wang, T.D. Spector, Obligatory and facilitative allelic variation in the DNA methylome within common disease-associated loci, Nat. Commun. 9 (2018) 8, https://doi.org/10.1038/s41467-017-01586-1.
- [20] Z. Wu, H. Wu, W. Cai, Z. Wen, B. Jia, L. Wang, W. Jin, T. Ma, Engineering bismuth-tin interface in bimetallic aerogel with a 3D porous structure for highly selective electrocatalytic CO<sub>2</sub> reduction to HCOOH, Angew. Chem. Int. Ed. 60 (2021) 12554–12559, https://doi.org/10.1002/anie.202102832.
- [21] Y. Liu, Z.X. Lou, X. Wu, B. Mei, J. Chen, J.Y. Zhao, J. Li, H.Y. Yuan, M. Zhu, S. Dai, C. Sun, P.F. Liu, Z. Jiang, H.G. Yang, Molecularly distorted local structure in Bi<sub>2</sub>CuO<sub>4</sub> oxide to stabilize lattice oxygen for efficient formate electrosynthesis, Adv. Mater. 34 (2022) 2202568, https://doi.org/10.1002/adma.202202568.
- [22] J. Zhu, J. Li, R. Lu, R. Yu, S. Zhao, C. Li, L. Lv, L. Xia, X. Chen, W. Cai, J. Meng, W. Zhang, X. Pan, X. Hong, Y. Dai, Y. Mao, J. Li, L. Zhou, G. He, Q. Pang, Y. Zhao, C. Xia, Z. Wang, L. Dai, L. Mai, Surface passivation for highly active, selective, stable, and scalable CO<sub>2</sub> electroreduction, Nat. Commun. 14 (2023) 4670, https://doi.org/10.1038/s41467-023-40342-6.
- [23] X. Yan, C. Chen, Y. Wu, S. Liu, Y. Chen, R. Feng, J. Zhang, B. Han, Efficient electroreduction of CO<sub>2</sub> to C<sub>2+</sub> products on CeO<sub>2</sub> modified CuO, Chem. Sci. 12 (2021) 6638–6645, https://doi.org/10.1039/d1sc01117k.
- [24] J. Jiao, Y. Ma, X. Han, A. Ergu, C. Zhang, P. Chen, W. Liu, Q. Luo, Z. Shi, H. Xu, C. Chen, Y. Li, T. Lu, Sun-simulated-driven production of high-purity methanol from carbon dioxide, Nat. Commun. 16 (2025) 857, https://doi.org/10.1038/s41457.025.61101.8
- [25] H. Yan, N. Zhang, D. Wang, Highly efficient CeO<sub>2</sub>-supported noble-metal catalysts: from single atoms to nanoclusters, Chem. Catal. 2 (2022) 1594–1623, https://doi. org/10.1016/j.checat.2022.05.001.
- [26] D. Gao, Y. Zhang, Z. Zhou, F. Cai, X. Zhao, W. Huang, Y. Li, J. Zhu, P. Liu, F. Yang, G. Wang, X. Bao, Enhancing CO<sub>2</sub> electroreduction with the metal–oxide interface, J. Am. Chem. Soc. 139 (2017) 5652–5655, https://doi.org/10.1021/jacs.7b00102.
- [27] R. Pang, P. Tian, H. Jiang, M. Zhu, X. Su, Y. Wang, X. Yang, Y. Zhu, L. Song, C. Li, Tracking structural evolution: operando regenerative  $CeO_x/Bi$  interface structure

- for high-performance CO<sub>2</sub> electroreduction, Natl. Sci. Rev. 8 (2021) nwaa187, https://doi.org/10.1093/nsr/nwaa187.
- [28] J. Jiao, Q. Yuan, M. Tan, X. Han, M. Gao, C. Zhang, X. Yang, Z. Shi, Y. Ma, H. Xiao, J. Zhang, T. Lu, Constructing asymmetric double-atomic sites for synergistic catalysis of electrochemical CO<sub>2</sub> reduction, Nat. Commun. 14 (2023) 6164, https://doi.org/10.1038/s41467-023-41863-w.
- [29] S. Yang, M. Jiang, W. Zhang, Y. Hu, J. Liang, Y. Wang, Z. Tie, Z. Jin, In situ structure refactoring of bismuth nanoflowers for highly selective electrochemical reduction of CO<sub>2</sub> to formate, Adv. Funct. Mater. 33 (2023) 2301984, https://doi. org/10.1002/adfm.202301984.
- [30] J. Chen, L. Wang, Effects of the catalyst dynamic changes and influence of the reaction environment on the performance of electrochemical CO<sub>2</sub> reduction, Adv. Mater. 34 (2022) 2103900, https://doi.org/10.1002/adma.202103900.
- [31] Z. Li, Y. Yang, H. Ding, Z. Li, L. Wang, X. Zhang, J. Li, W. Xie, X. Hu, B. Wang, M. Wei, In situ investigations on Bi-based electrocatalyst construction and reaction dynamic monitoring toward efficient CO<sub>2</sub> reduction, Chem. Catal. 3 (2023) 100767, https://doi.org/10.1016/j.checat.2023.100767.
- [32] C. Xia, P. Zhu, Q. Jiang, Y. Pan, W. Liang, E. Stavitski, H.N. Alshareef, H. Wang, Continuous production of pure liquid fuel solutions via electrocatalytic CO<sub>2</sub> reduction using solid-electrolyte devices, Nat. Energy 4 (2019) 776–785, https://doi.org/10.1038/s41560-019-0451-x.
- [33] L. Fan, C. Xia, P. Zhu, Y. Lu, H. Wang, Electrochemical CO<sub>2</sub> reduction to high-concentration pure formic acid solutions in an all-solid-state reactor, Nat. Commun. 11 (2020) 3633, https://doi.org/10.1038/s41467-020-17403-1.
- [34] T. Zheng, C. Liu, C. Guo, M. Zhang, X. Li, Q. Jiang, W. Xue, H. Li, A. Li, C. Pao, J. Xiao, C. Xia, J. Zeng, Copper-catalysed exclusive CO<sub>2</sub> to pure formic acid conversion via single-atom alloying, Nat. Nanotechnol. 16 (2021) 1386–1393, https://doi.org/10.1038/s41565-021-00974-5.
- [35] L. Lin, X. He, X. Zhang, W. Ma, B. Zhang, D. Wei, S. Xie, Q. Zhang, X. Yi, Y. Wang, A nanocomposite of bismuth clusters and Bi<sub>2</sub>O<sub>2</sub>CO<sub>3</sub> sheets for highly efficient electrocatalytic reduction of CO<sub>2</sub> to formate, Angew. Chem. Int. Ed. 62 (2023) e202214959, https://doi.org/10.1002/anie.202214959.
- [36] J. Hafner, G. Kresse, Ab initio molecular-dynamics simulation of the liquid-metal-amorphous-semiconductor transition in germanium, J. Phys. Rev. B 49 (1994) 14251–14269, https://doi.org/10.1103/PhysRevB.49.14251.
- [37] J. Furthmüller, G. Kresse, Efficient iterative schemes for ab initio total-energy calculations using a plane-wave basis set, J. Phys. Rev. B 54 (1996) 11169–11186, https://doi.org/10.1103/PhysRevB.54.11169.
- [38] K. Burke, M. Ernzerhof, J.P. Perdew, Generalized gradient approximation made simple, Phys. Rev. Lett. 77 (1996) 3865–3868, https://doi.org/10.1103/ PhysRevLett 77 3865
- [39] P.E. Blöchl, Projector augmented-wave method, J. Phys. Rev. B 50 (1994) 17953–17979, https://doi.org/10.1103/PhysRevB.50.17953.
- [40] Q. Zhang, K. Lian, G. Qi, S. Zhang, Q. Liu, Y. Luo, J. Luo, X. Liu, High-entropy alloys in water electrolysis: recent advances, fundamentals, and challenges, Sci. China-Mater. 66 (2023) 1681–1701, https://doi.org/10.1007/s40843-022-2379-8.
- [41] N. Sun, S. Ru, C. Zhang, W. Liu, Q. Luo, J. Jiao, T. Lu, Promoting oxygen reduction reaction by tuning externally doped nitrogen around atomically dispersed iron, Fundam. Res. 5 (2025) 1488–1494. https://doi.org/10.1016/j.fmre.2022.07.014.
- Fundam. Res. 5 (2025) 1488–1494, https://doi.org/10.1016/j.fmre.2022.07.014.

  [42] R. Cui, Q. Yuan, C. Zhang, X. Yang, Z. Ji, Z. Shi, X. Han, Y. Wang, J. Jiao, T. Lu, Revealing the behavior of interfacial water in Te-doped Bi via operando infrared spectroscopy for improving electrochemical CO<sub>2</sub> reduction, ACS Catal. 12 (2022) 11294–11300. https://doi.org/10.1021/acscatal.2c03369.
- [43] L. Sun, X. Liang, H. Liu, H. Cao, X. Liu, Y. Jin, X. Li, S. Chen, X. Wu, Activation of Co-O bond in (110) facet exposed Co<sub>3</sub>O<sub>4</sub> by Cu doping for the boost of propane catalytic oxidation, J. Hazard. Mater. 452 (2023) 131319, https://doi.org/ 10.1016/j.jhazmat.2023.131319.
- [44] Y. Duan, Y. Zhou, Z. Yu, D. Liu, Z. Wen, J. Yan, Q. Jiang, Boosting production of HCOOH from CO<sub>2</sub> electroreduction via Bi/CeO, Angew. Chem. Int. Ed. 60 (2021) 8798–8802, https://doi.org/10.1002/anie.202015713.
- [45] Y. Song, X. Zhang, Z. Xiao, Y. Wang, P. Yi, M. Huang, L. Zhang, Coupled amorphous NiFeP/cystalline Ni<sub>3</sub>S<sub>2</sub> nanosheets enables accelerated reaction kinetics for high current density seawater electrolysis, Appl. Catal. B Environ. 352 (2024) 124028, https://doi.org/10.1016/j.apcatb.2024.124028.
- [46] Y. Wang, X. Zheng, D. Wang, Design concept for electrocatalysts, Nano Res. 15 (2022) 1730–1752, https://doi.org/10.1007/s12274-021-3794-0.
- [47] S. Xie, S. Tian, J. Yang, N. Wang, Q. Wan, M. Wang, J. Liu, J. Zhou, P. Qi, K. Sui, X. Li, D. Ma, X.S. Zhao, Synergizing Mg single atoms and Ru nanoclusters for boosting the ammonia borane hydrolysis to produce hydrogen, Angew. Chem. Int. Ed. 64 (2025) e202424316, https://doi.org/10.1002/anie.202424316.
- [48] M.A. Laguna-Marco, C. Piquer, A.G. Roca, R. Boada, M. Andrés-Vergés, S. Veintemillas-Verdaguer, C.J. Serna, A. Iadecola, J. Chaboy, Structural determination of Bi-doped magnetite multifunctional nanoparticles for contrast imaging, Phys. Chem. Chem. Phys. 16 (2014) 18301–18310, https://doi.org/ 10.1039/C4CP01392A.
- [49] H. Shi, R. Shao, S. Lei, M. Zhou, X. Yuan, Z. Chen, S. Wei, S. Zhong, Y. Zhao, L. Zhao, S. Bai, Breaking Janus shells in hollow heterostructured photocatalysts with spatially separated redox sites for enhanced synergy of CO<sub>2</sub> methanation and H<sub>2</sub>O oxidation, Appl. Catal. B Environ. 373 (2025) 125363, https://doi.org/ 10.1016/j.apcatb.2025.125363.

- [50] D. Song, Y. Lian, M. Wang, Y. Su, F. Lyu, Z. Deng, Y. Peng, Electrochemical CO2 reduction catalyzed by organic/inorganic hybrids, eScience 3 (2023) 100097,
- https://doi.org/10.1016/j.esci.2023.100097,

  [51] H. Zhao, Y. Xie, B. Lv, G. Jing, Y. Li, Achieving current density of 815 mA/cm<sup>2</sup> for electrochemical CO2 reduction to formate by enhancing \*OCHO intermediate
- adsorption through intercalated Bi single atoms in BiOBr, Appl. Catal. B Environ.
- 371 (2025) 125234, https://doi.org/10.1016/j.apcatb.2025.125234. [52] Y. Li, E.P. Delmo, G. Hou, X. Cui, M. Zhao, Z. Tian, Y. Zhang, M. Shao, Enhancing Local CO<sub>2</sub> adsorption by L-histidine incorporation for selective formate production over the wide potential window, Angew. Chem. Int. Ed. 62 (2023) e202313522, https://doi.org/10.1002/anie.202313522.